



OPEN

Comprehensive analysis identifies ubiquitin ligase FBXO42 as a tumor-promoting factor in neuroblastoma

Jianwu Zhou¹, Qijun Li², Xiaobin Deng¹, Liang Peng¹, Jian Sun¹, Yao Zhang¹ & Yifei Du¹✉

Neuroblastoma, the deadliest solid tumor in children, exhibits alarming mortality rates, particularly among high-risk cases. To enhance survival rates, a more precise risk stratification for patients is imperative. Utilizing proteomic data from 34 cases with or without N-Myc amplification, we identified 28 differentially expressed ubiquitination-related proteins (URGs). From these, a prognostic signature comprising 6 URGs was constructed. A nomogram incorporating clinical-pathological parameters yielded impressive AUC values of 0.88, 0.93, and 0.95 at 1, 3, and 5 years, respectively. Functional experiments targeting the E3 ubiquitin ligase FBXO42, a component of the prognostic signature, revealed its TP53-dependent promotion of neuroblastoma cell proliferation. In conclusion, our ubiquitination-related prognostic model robustly predicts patient outcomes, guiding clinical decisions. Additionally, the newfound pro-proliferative role of FBXO42 offers a novel foundation for understanding the molecular mechanisms of neuroblastoma.

Keywords Neuroblastoma, Bioinformatics, FBXO42, TP53, Proliferation

Neuroblastoma (NB), the most prevalent extracranial solid tumor in children, constitutes 15% of childhood cancer-related deaths^{1,2}. Risk stratification schemes currently used in clinical practice mainly depend on integrating single prognostic factors, including factors such as age, tumor stage, mitotic-karyorrhexis index, N-Myc amplification, and ALK expression³. The advent of novel patient stratification approaches, therapies, and drugs has significantly elevated the long-term survival rate of children with high-risk NB to 50%^{3,4}. However, these patients frequently confront refractory tumors and disease relapse, displaying suboptimal responses to additional treatments⁵. Consequently, enhancing risk stratification and gaining deeper insights into the molecular mechanisms of NB are imperative to augment treatment efficacy and improve patient survival rates.

Ubiquitination is a post-translational modification occurring after protein translation, facilitated by E1 activating enzymes, E2 conjugating enzymes, and E3 ligases, resulting in ubiquitin-modified proteins^{6–8}. Ubiquitin, with seven lysine residues, can form mono-ubiquitination or poly-ubiquitination on proteins⁹. This modification process is reversible through deubiquitinating enzymes¹⁰. One of the primary functions of ubiquitination is to promote protein degradation, regulating various cellular processes, including tumor progression and treatment resistance^{11,12}. Ubiquitination not only plays a crucial role in neuroblastoma but is also widely implicated in the occurrence and development of various cancers, providing novel therapeutic avenues^{13,14}. Studies have identified the relevance of ubiquitination to neuroblastoma, such as HAUSP deubiquitinating and stabilizing N-Myc in neuroblastoma cells¹⁵, Trim32 promoting degradation of MYCN on the spindle poles and inducing asymmetric cell division in human neuroblastoma cells¹⁶, and hyperubiquitination of wild-type p53 contributing to cytoplasmic sequestration in neuroblastoma¹⁷. Previous studies have explored the risk features of ubiquitination-related genes in pancreatic cancer, ovarian cancer, and hepatocellular carcinoma, and the prognostic models constructed based on these genes have been effective in predicting patient outcomes^{18–20}. Despite the development of numerous prognostic models for risk stratification in neuroblastoma^{21–23}, the risk characteristics of ubiquitination-related genes in neuroblastoma have not been revealed. Therefore, it is necessary to explore the role of ubiquitination-related genes in the prognosis of neuroblastoma patients.

¹Department of Pediatric Surgical Oncology, Children's Hospital of Chongqing Medical University; and the National Clinical Research Center for Child Health and Disorders, Ministry of Education Key Laboratory of Child Development and Disorders, Chongqing Key Laboratory of Pediatrics, Chongqing 400014, People's Republic of China. ²Laboratory Animal Center, Chongqing Medical University, Chongqing 400016, People's Republic of China. ✉email: doephy@163.com

Here, we analyzed differentially expressed proteins in the N-Myc amplified group from proteomic data, which were evaluated for prognostic features in transcriptomic data. We developed ubiquitination-related prognostic features, including UHRF1, KEAP1, FBXO42, UFL1, RNF213, and BRCK1. The ubiquitination prognostic model identified a high-risk population with poorer immune therapy outcomes and prognosis, aiding in the formulation of personalized treatment and follow-up plans by physicians. Additionally, to explore the potential mechanisms of ubiquitin–proteasome regulation in neuroblastoma, we predicted substrate proteins of FBXO42 and conducted bioinformatics and cellular functional analyses. This study presents an innovative ubiquitination gene risk signature for neuroblastoma and offers novel insights into assessing the role of the ubiquitination gene FBXO42 in neuroblastoma.

Materials and methods

Data resources

Proteomic data for neuroblastoma were obtained from the study by Hartlieb et al.²⁴. The gene expression data (GSE62564) were annotated based on GPL11154 (accessed on <https://www.ncbi.nlm.nih.gov/geo/> on December 25, 2023). GSE62564 comprises 498 neuroblastoma samples, including clinical information such as gender, age, International Neuroblastoma Staging System (INSS) stage, N-Myc amplification status, COG risk stratification, and overall survival²⁵. Ensemble IDs were converted to corresponding gene symbols using the cluster Profiler R package. Subsequently, the gene expression matrix underwent quantile normalization and log₂ transformation for further analysis.

Selection of differentially expressed proteins related to ubiquitination

Ubiquitination modification is a post-transcriptional protein regulation, so the proteomics data cohort was used for differential screening. E3 ubiquitin ligases and deubiquitinases were extracted from the UbiBrowser 2.0 webpage (http://ubibrowser.bio-it.cn/ubibrowser_v3/, accessed on December 25, 2023) to identify differentially expressed proteins related to ubiquitination (URG)²⁶. Differential expression analysis of proteomic data was conducted using the R2 tool (<https://hgserver1.amc.nl/cgi-bin/r2/main.cgi>, accessed on December 25, 2023) to identify proteins exhibiting differential expression between N-Myc amplification and non-amplification groups based on Fold change > 1 and FDR < 0.01. The internal ID on the R2 website is "internal identifier: ps_avgpres_fw2010prot34_fw2010prot", and the number of samples is 34. Patient characteristics were supplemented in the revised manuscript as Supplementary table 1, including 12 MYCN amplified and 22 non-amplified patients.

Functional enrichment analysis and construction of protein–protein interaction network

Enrichment analysis of ubiquitination-related genes (URG) was conducted using DAVID (v.6.8, <https://david.ncicrf.gov/>, accessed on December 25, 2023) to gain preliminary insights into the biological functions of these genes. The KEGG pathway database was derived from entries compiled by the Kanehisa laboratory^{27–29}. Significance was determined at $p < 0.05$ and FDR < 25%. The STRING database (v 11.0, <https://string-db.org>, accessed on December 25, 2023) was employed for constructing the protein–protein interaction (PPI) network.

Construction of prognostic scores for ubiquitination-related genes

Increasing the sample size can enhance the prognostic performance of models; hence, we utilized the larger GSE62564 dataset to construct the LASSO regression model. This study employed the shrinkage estimation method LASSO, which identifies differentially expressed genes (DEGs) associated with overall survival by constraining certain feature coefficients to zero and minimizing the sum of squared residuals under these constraints. The LASSO Cox regression model from the "glmnet" R package was utilized. Subsequently, we obtained risk scores for each gene at the optimal λ value, calculated as the sum of each gene's expression level multiplied by the corresponding β coefficient. Patients were stratified into high and low-risk groups based on the median cutoff of risk scores. The prognostic ability of risk scores was evaluated through Kaplan–Meier analysis and ROC curve assessment.

Gene set enrichment analysis (GSEA) and ubiquitination modification substrate prediction

For Gene set enrichment analysis (GSEA), we obtained the GSEA software (version 3.0) from the GSEA website (<https://www.gsea-msigdb.org/gsea>, accessed on December 25, 2023)³⁰. The samples were divided into two groups according to risk scores, and the c2.cp.kegg.v7.4.symbols.gmt subcollection was downloaded from the Molecular Signatures Database (<http://www.gsea-msigdb.org/gsea/downloads.jsp>) to evaluate related pathways and molecular mechanisms³¹. Based on the gene expression profile and phenotype grouping, the minimum gene set was set to 5, the maximum gene set was 5000, and one thousand resampling were performed. P value of < 0.01 and a FDR of < 0.25 were considered statistically significant. UbiBrowser 2.0 (http://ubibrowser.bio-it.cn/ubibrowser_v3/, accessed on December 25, 2023) was employed for predicting substrate proteins of FBXO42²⁶.

Immune infiltration and immune microenvironment assessment

The immune microenvironment features between the high-risk and low-risk groups were assessed using ESTIMATE (<https://sourceforge.net/projects/estimateproject/>, accessed on December 25, 2023)³². Additionally, immune cell infiltration characteristics were evaluated between the high-risk and low-risk groups using CIBERSORT (<https://cibersortx.stanford.edu/>, accessed on December 25, 2023) and EPIC (Immune Cell <http://epic.gfellerlab.org/>, accessed on December 25, 2023)^{33,34}. The TIDE scores status of NB samples were calculated utilizing the Tumor Immune Dysfunction and Exclusion (TIDE <http://tide.dfci.harvard.edu/login/>, accessed on December 25, 2023) database³⁵.

Protein structure prediction and gene mutation analysis

Protein structure prediction was performed by uploading gene symbols to genecard (<https://www.genecards.org/>, accessed on December 25, 2023), and protein structure was predicted using AlphaFold connected to it. Gene mutation analysis was performed by uploading gene symbols to cbiportal (<https://www.cbiportal.org/>, accessed on December 25, 2023), and the cohort used was Pediatric Neuroblastoma (TARGET, 2018).

Plasmid construction and cell transfection

The coding sequence (CDS) of FBXO42 (XM_047422747.1) was amplified from HEK293T cell cDNA through polymerase chain reaction (PCR) in vitro, using the primer sequences FBXO42-F: AAAGGATCCGAATTCatg-gccagctcctcggacagtg and FBXO42-R: ATGGTGGTGTCTCGAGttatctcttctcgtacaagtaca. Subsequently, the amplified sequence was cloned into the CMV-flag vector using EcoRI and XhoI restriction enzymes. The CMV-flag- FBXO42 plasmid was sequenced and aligned to confirm complete cloning of the DNA sequence (BGI, Chongqing, China).

SiRNA oligonucleotides targeting FBXO42, synthesized by BGI (Chongqing, China), were transfected into cells using Lipofectamine 2000 at a final concentration of 20 nM. The SH-SY5Y and SK-N-SH cells were cultured in Dulbecco's Modified Eagle Medium (DMEM) supplemented with 10% fetal bovine serum (Gibco, Carlsbad, CA, USA) and 1% penicillin/streptomycin (PS) (Invitrogen, Grand Island, NY, USA). Cells were maintained in a 5% CO₂ incubator at 37 °C. Following the manufacturer's protocol, Neofect™ DNA transfection reagent (Neofect Biotech, Beijing, China) was used to transfect Flag-CTL or Flag-FBXO42 plasmids into cells. In brief, cells were cultured in complete medium in a 35 mm culture dish, DNA (2 µg) was diluted in DMEM, 2 µL Neofect™ was added, mixed gently, and incubated at room temperature for 15 min. The transfection mixture was then added to the dish and incubated at 37 °C with 5% CO₂.

Protein immunoblot analysis

Following transfection with Flag-CTL and Flag-FBXO42 plasmids for 48 h, SH-SY5Y and SK-N-SH cells were lysed in 1% SDS lysis buffer containing a protease inhibitor cocktail and a phosphatase inhibitor cocktail (Apexbio, Houston, TX, USA) for protein immunoblot analysis. Protein concentration was determined using the BCA protein assay kit (Thermo Scientific, Waltham, MA, USA). Immunoblots were probed with primary antibodies against P53, AKT, p-AKT (1:1000, Abcam, Shanghai, China), ERK, p-ERK, Caspase 3, Cleaved Caspase 3, P65, p-P65, Caspase 9 (1:1000, Cell Signaling Technology, MA, USA), FBXO42 (1:2000, NOVUS, MA, USA), and β-Actin (1:4000, Proteintech, Wuhan, China). Visualization of bands was performed using ECL reagent (Smart-Lifesciences, Changzhou, China).

Real-time quantitative PCR (RT-qPCR)

RT-qPCR was conducted following the methodology described by Shao et al.²². Specifically, total RNA was extracted from cells using TRIzol reagent (Invitrogen), following the manufacturer's instructions. For each sample, 1 µg of total RNA was used for cDNA synthesis in a 20 µL reaction system with the iScript cDNA synthesis kit (Bio-Rad). Subsequently, a 25 µL PCR reaction was performed using 1 µL cDNA library from each sample. Fast SYBR Green Master Mix (Bio-Rad) was employed, and the cycle threshold (Ct) for each sample was determined using the CFX96 Real-time PCR detection system (Bio-Rad). The 18S gene served as the standardized reference gene. The relative expression level of the target gene was calculated using the 2^{-ΔΔCt} method (ΔCt = Ct of 18S - Ct of the target gene). The primer sequences used were as follows: TP53-F: AAGTCTAGAGCCACC GTCCA, TP53-R: CTGGCATTCTGGGAGCTTCA ; FBXO42-F: CCTTTCTCTCACCGTATCAGGAACAC, FBXO42-R: AGCATCATAATAGCATGCACTGTGCG; 18S F: GTAACCCGTTGAACCCCAT, 18S R: CCA TCCAATCGGTAGTAGCG.

Colony formation assay

Long-term cell survival was assessed through a colony formation assay. Briefly, 1000 cells were seeded into 6-well plates and allowed to grow for 2 weeks. The cells were fixed with 4% paraformaldehyde for 15 min and visualized by 0.5% (w/v) crystal violet (Sigma-Aldrich) staining. Colonies on the plate were scanned using the Odyssey Scanner (LI-COR, Lincoln, NE, USA), and the number of colonies was quantified using Image J software.

Cell viability assay

Cell viability analysis was performed 48 h post-transfection using the Cell Counting Kit-8 (CCK-8) assay kit (MedChem Express, NJ, USA). Flag-CTL or Flag-FBXO42 cells were seeded at a density of 2 × 10⁴ cells per well in a 96-well plate and cultured for 12 h. Subsequently, DMEM medium (100 µL) and CCK8 solution (10 µL) were added to each well and incubated for 1 h. Finally, absorbance at 450 nm was measured using a microplate reader (Thermo Scientific, Waltham, MA, USA). Statistical analyses were performed using GraphPad Prism 5 software (GraphPad, San Diego, CA, USA) with paired or unpaired t-tests, as appropriate.

Statistical analysis

Statistical analysis was conducted using R 4.0.2. Non-parametric tests were employed to assess differences in immune features between the two risk groups and the differential expression of FBXO42 among different clinical-pathological parameter groups. Kaplan–Meier analysis was utilized to compare survival status among groups, and ROC curve analysis was performed to evaluate the predictive ability of the model. Unless otherwise stated, *p* < 0.05 was considered statistically significant.

Result

Identification of aberrantly ubiquitinated proteins in N-Myc amplified neuroblastoma

Proteomic data from 34 neuroblastoma samples were analyzed based on the N-Myc amplification status, guided by the study conducted by Hartlieb²⁴. The differential expression analysis, utilizing criteria of Log₂ fold absolute value > 1 and FDR < 0.01, revealed significant alterations in protein expression within the N-Myc amplified group, comprising 235 upregulated and 375 downregulated proteins (Fig. 1A, Supplementary table 2). Leveraging the findings from Wang et al.'s research²⁶, which identified 660 E3 ubiquitin ligases and 112 deubiquitinases, 28 differentially expressed proteins associated with ubiquitination modifications (URG) were extracted (Fig. 1B, Supplementary table 3). Functional enrichment analysis of the 610 differentially expressed proteins unveiled their involvement in biological processes such as the establishment of localization, transport, and cellular protein metabolic processes (Fig. 1C). Furthermore, these proteins were predominantly localized in the cell cytosol, vesicles, and non-membrane-bounded organelles (Fig. 1D), exhibiting key molecular functions related to catalytic activity, anion binding, and small molecule binding (Fig. 1E). Of particular interest in KEGG pathway analysis were the highly enriched categories of Metabolic pathways, Endocytosis, and Ribosome biogenesis in eukaryotes (Fig. 1F), providing valuable insights into the molecular mechanisms underlying neuroblastoma.

Establishment of a URG-based signature in neuroblastoma

LASSO Cox regression analysis was conducted to establish a signature based on Ubiquitination-Related Genes (URG) in neuroblastoma. Leveraging the largest known transcriptomic research dataset for neuroblastoma³⁶, 28 URGs were included in the LASSO Cox regression analysis, employing a tenfold cross-validation to obtain the optimal model (Fig. 2A,B). Setting the Lambda value at 0.0161, we derived a model formula comprising 13 genes:

$$\begin{aligned} \text{RiskScore} = & -0.092 * \text{GNB5} - 0.120 * \text{HECW2} + 0.416 * \text{UFL1} \\ & + 0.261 * \text{DCAF13} + 0.577 * \text{PRPF4} - 0.816 * \text{FBXO42} \\ & - 0.044 * \text{HECW1} + 0.161 * \text{PWP2} + 0.444 * \text{UHRF1} \\ & + 0.866 * \text{KEAP1} + 0.210 * \text{RNF213} + 0.162 * \text{RBCK1} \\ & - 0.140 * \text{USP24}. \end{aligned}$$

Patients were stratified into high and low URG score groups based on the median URG score (Fig. 2C). Comparative analysis revealed that patients with higher URG scores experienced poorer overall survival (OS) than those in the low URG score group (Fig. 2D, E). Furthermore, elevated expressions of genes such as DCAF13, PRPF4, PWP2, UHRF1, and KEAP1 were associated with adverse prognosis, while the opposite trend was observed for other genes (Fig. 2F). Additionally, the URG score demonstrated robust predictive ability with AUC values of 0.89, 0.90, and 0.91 at 1 year, 3 years, and 5 years, respectively (Fig. 2G).

Further optimization of URG score through multifactorial COX regression analysis

In the pursuit of cost-effectiveness for patients and to better serve clinical needs, it is essential to minimize the number of genes constituting the model while ensuring that the prognostic efficacy is not compromised. Consequently, the 13 genes within the URG score underwent additional multifactorial COX regression analysis, leading to the identification of 6 genes, namely UHRF1, KEAP1, FBXO42, UFL1, RNF213, and RBCK1. The final model formula, comprising these 6 genes, is expressed as follows (Fig. 3A):

$$\begin{aligned} \text{RiskScore} = & 0.444 * \text{UHRF1} + 0.866 * \text{KEAP1} - 0.816 * \text{FBXO42} \\ & + 0.419 * \text{UFL1} + 0.210 * \text{RNF213} + 0.162 * \text{RBCK1}. \end{aligned}$$

Evidently, the URG score based on these 6 genes remains effective in distinguishing samples with favorable and unfavorable prognoses (Fig. 3B). Importantly, the new URG score exhibited AUC values of 0.88, 0.90, and 0.92 at 1 year, 3 years, and 5 years, respectively (Fig. 2G, 3C), showing minimal difference compared to the original 13-gene URG score. In fact, these 6 genes can also serve as independent prognostic factors for discriminating samples with favorable and unfavorable outcomes (Fig. 3D–I).

Construction of nomogram based on URG score

Prior studies have indicated that constructing nomograms by integrating clinical-pathological parameters enhances the accuracy of prognosis prediction for clinical patients^{23,37}. A column line chart, encompassing clinical features and the URG score, was established to predict the overall survival (OS) of patients in the GSE49711 cohort (Fig. 4A). Kaplan–Meier survival curves demonstrate the superior prognostic discrimination ability of the nomogram (Fig. 4B). Furthermore, compared to the original URG score, the nomogram exhibited increased AUC values, reaching 0.88, 0.93, and 0.95 at 1 year, 3 years, and 5 years, respectively (Fig. 4C). However, while the calibration curve indicates excellent predictive performance, suggesting optimal applicability and accuracy of our risk model, it is essential to note that the nomogram might overestimate the 1-year survival rate (Fig. 4D) and slightly underestimate the 3-year and 5-year survival rates (Fig. 4E,F) in practical applications.

Evaluation of immune infiltration, microenvironment, and response in two risk groups

To assess the relevance of the risk model in immune therapeutic strategies, four immune evaluation methods were employed to estimate the immune status of the two risk groups. The Estimate algorithm computed that individuals in the high-risk group exhibited lower stromal score, estimate score, and immune score (Fig. 5A–C,

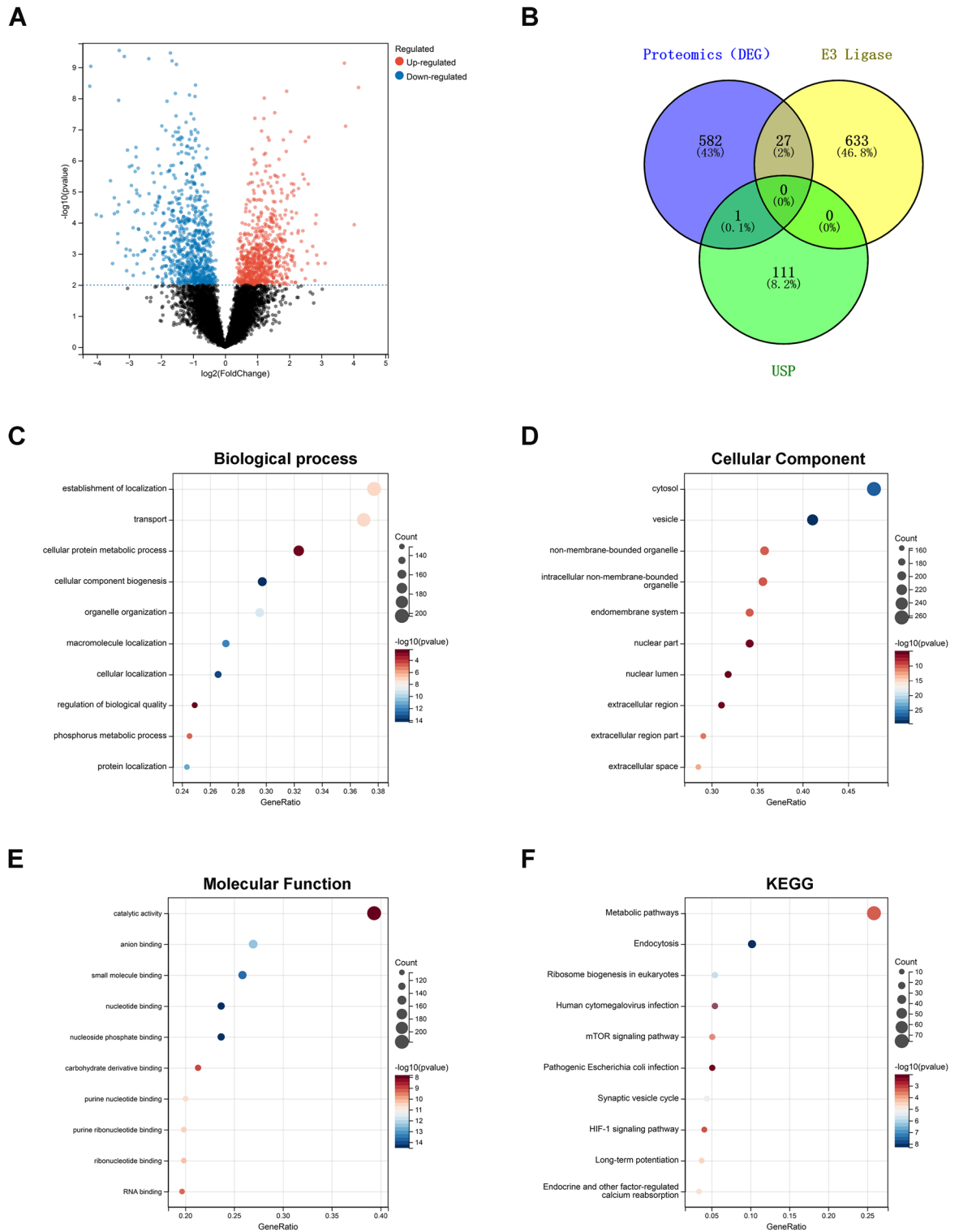


Figure 1. Discovery of ubiquitination-related differential proteins and aberrant pathways in N-Myc amplified neuroblastoma. **(A)** Volcano plot of differentially expressed proteins in the proteomic dataset of 34 cases. The x-axis represents the fold change in gene expression, and the y-axis represents FDR. Red and blue dots indicate significantly upregulated and downregulated genes, respectively. **(B)** Venn diagram of differentially expressed proteins, E3 ubiquitin ligases, and deubiquitinases. **(C,D)** Gene Ontology (GO) analysis of 610 differentially expressed proteins, including biological process, cellular component, and molecular function. **(F)** Kyoto Encyclopedia of Genes and Genomes (KEGG) analysis of the 610 differentially expressed proteins.

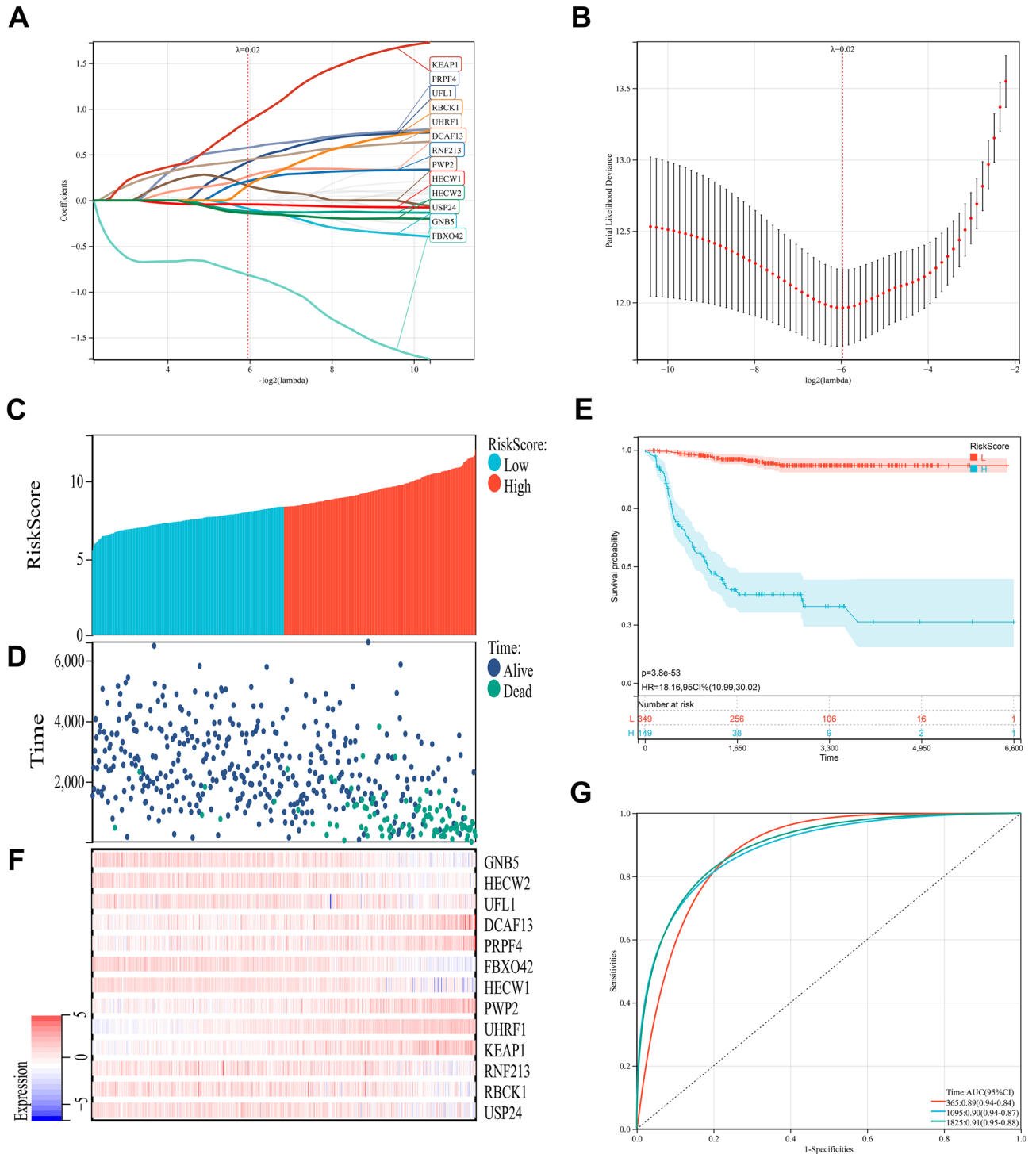


Figure 2. Development of the ubiquitination gene prognostic model. **(A)** Lasso coefficient plot of 28 prognostic-related ubiquitination genes in the Discovery (GSE62564 microarray) dataset. Grey represents eliminated genes. **(B)** Partial likelihood deviance of variables revealed by Lasso regression. Red dots indicate partial likelihood deviance values, grey lines represent standard errors (SE), and left and right vertical dashed lines represent the minimum standard with 1-SE standard and optimal values. **(C,D)** Distribution of risk scores **(C)** and survival status of patients **(D)** for the 13-gene prognostic model. **(E)** Kaplan–Meier analysis of the 13-gene risk score. **(F)** Heatmap showing the expression of the 13 feature genes (R 4.0.2, R package “pheatmap”). **(G)** ROC curve analysis of the 13-gene risk score.

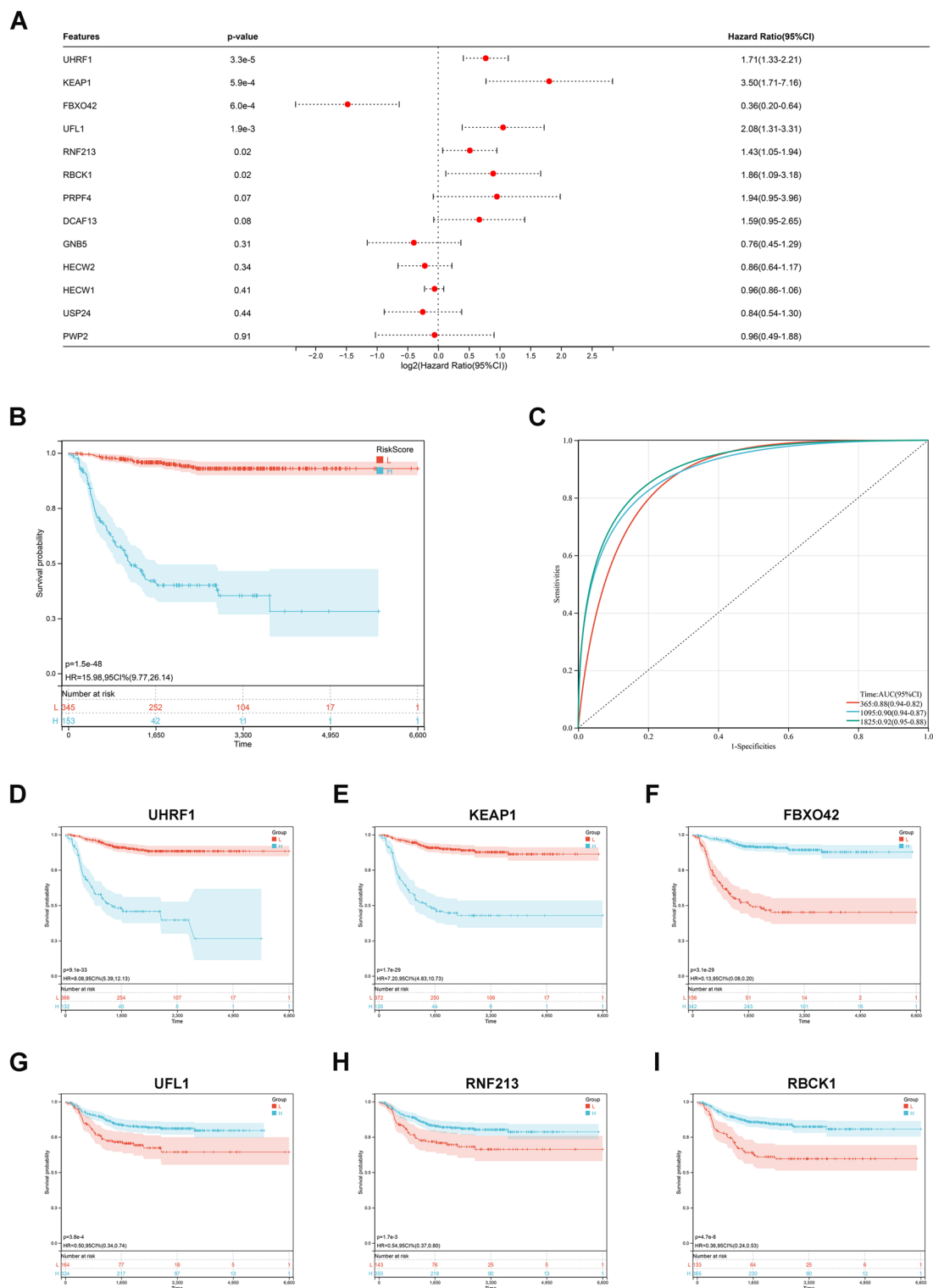


Figure 3. Further Optimization of the Risk Score using COX multivariate regression. (A) Multivariate Cox regression analysis of the 13 genes. (B) Kaplan–Meier analysis of the new 6-gene prognostic risk score. (C) ROC curve analysis of the new 6-gene prognostic risk score. (D–I) Kaplan–Meier analysis of UHRF (D), KEAP1 (E), FBXO42 (F), UFL1 (G), RNF213 (H), and RBCK1 (I) for the 6-gene risk score.

Supplementary table 4). The Cibersort algorithm evaluated the immune cell infiltration status of the two risk groups. The high-risk group showed lower levels of immune cell infiltration, specifically, distinct infiltration states were observed for memory B cells, plasma cells, Tregs, NK cells, and macrophages (Fig. 5D, Supplementary

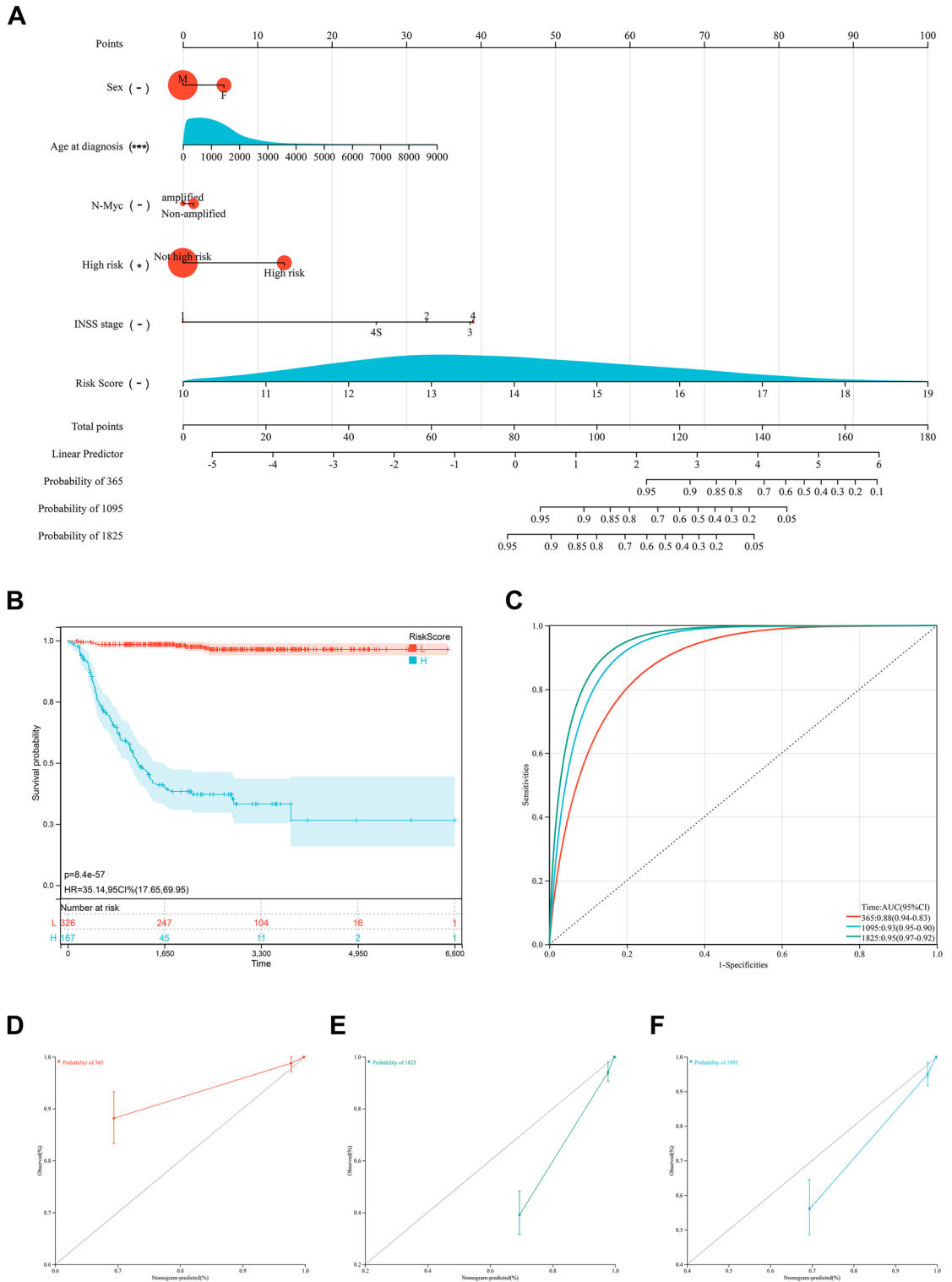


Figure 4. Construction and performance evaluation of nomogram. **(A)** Construction of a collagen nomogram in the GSE62564 dataset, including gender, age at diagnosis, N-Myc amplification status, COG risk stratification, INSS stage, and risk score. **(B,C)** Kaplan–Meier survival curve **(B)** and ROC curve **(C)** of the nomogram model in the GSE62564 dataset. **(D,F)** Calibration curves predicting 1, 3, and 5-year survival rates for the nomogram model. In the calibration curves, the diagonal grey dashed line represents a perfect predictive model, and the colored solid line represents the nomogram. A closer alignment of the red solid line to the grey dashed line indicates better predictive performance. –, $P > 0.05$; *, $P < 0.05$; ***, $P < 0.001$.

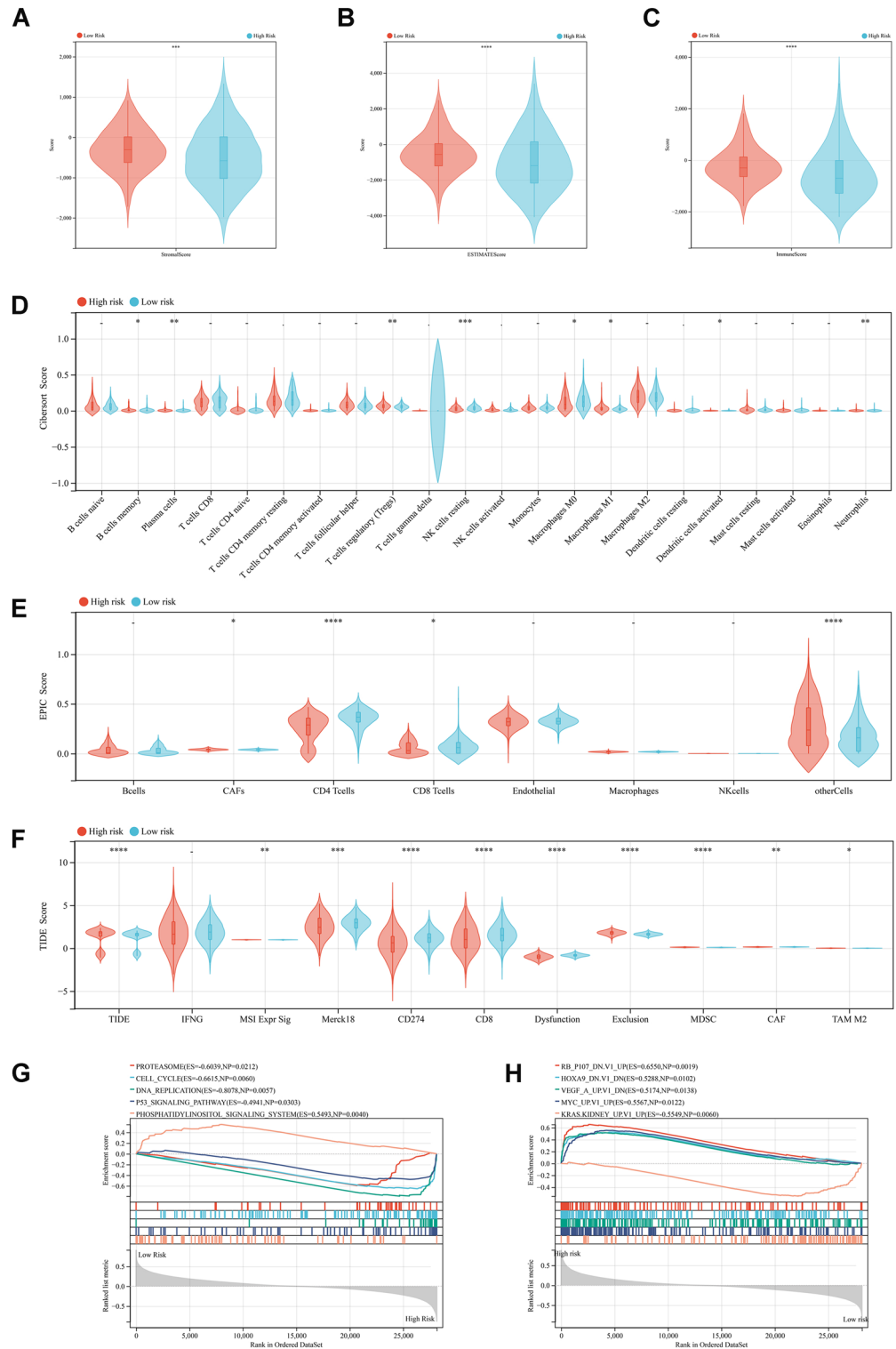


Figure 5. Immune status evaluation between high and low-risk groups by the nomogram model. (A–C) ESTIMATE algorithm assessing immune stroma (A), immune cells (B), and overall immune score (C) in two groups. (D,E) Cibersort and EPIC algorithms assessing 22 (D) and 8 (E) immune cell infiltration statuses in both groups. (F) TIDE algorithm estimating immune treatment response and prognosis. (G,H) Gene Set Enrichment Analysis (GSEA) of KEGG pathways (G) and oncology features (H) in the two risk groups.

table 5). Additionally, the EPIC algorithm was utilized to assess the infiltration levels of eight immune cell types, revealing lower infiltration levels of CAFs, CD4 T cells, and CD8 T cells in the high-risk group (Fig. 5E, Supplementary table 6).

Subsequently, the TIDE algorithm was employed to calculate the TIDE values and other relevant immune statuses for each patient in the cohort. TIDE scores indicated a higher likelihood of immune escape in the high-risk group, and other scores (such as MSI Expr Sig, Merck18, Dysfunction, and Exclusion) suggested potential immune therapeutic resistance in the high-risk group. Notably, the expression levels of CD274 (PD-1) and CD8 were lower in the high-risk group, further supporting the notion of poorer immune therapeutic prognosis in this group (Fig. 5F, Supplementary table 7). Furthermore, in the high-risk group samples, there was enhancement in phosphatidylinositol signaling, while signals related to cell cycle, DNA replication, P53, and proteasome were weakened (Fig. 5G, Supplementary table 8). Tumor characteristic assessment of the two risk groups revealed downregulation of KRAS KIDNEY features and upregulation of RB, HOXA9, VEGF, and MYC features in the high-risk group (Fig. 5H, Supplementary table 9).

E3 ubiquitin ligase FBXO42's anticancer role in neuroblastoma?

In the preceding multifactorial Cox regression analysis (Fig. 3A), six genes were identified as risk factors for neuroblastoma (NB) patients, excluding FBXO42. FBXO42, a member of the F-box protein family characterized by an approximately 40-amino acid F-box motif (Fig. 6A), was further investigated for its expression patterns and potential anticancer effects. Deep deletion is the only genetic mutation state of FBXO42 in NB, and the probability of occurrence is less than 1% (Fig. 6B). Additionally, immunofluorescence and immunohistochemistry results from the HPA database indicated that FBXO42 predominantly localizes to the cell nucleus and shows moderate expression in the adrenal gland (Fig. 6C,D). Furthermore, FBXO42 displayed lower expression in the high-risk group and N-Myc amplification group within the COG risk stratification (Fig. 6E,F), irrespective of gender (Fig. 6G). Importantly, patients with high FBXO42 expression seemed to have a better INSS stage (Fig. 6H). Specifically, patients with a poorer prognosis in stage 4 exhibited differential FBXO42 expression compared to patients in other stages. Moreover, the expression pattern of FBXO42 in stage 2 patients resembled that of stage 4 patients, while no significant difference in FBXO42 expression was observed between stage 2 and stage 1 patients. Subsequently, the String database query results indicated potential interactions of FBXO42 with 10 proteins (Fig. 6I), possibly involved in the cell cycle, ubiquitin-mediated protein degradation, Wnt signaling pathway (Fig. 6J), as well as processes such as protein-containing complex formation and cellular protein modification (Fig. 6L). In conclusion, the results of bioinformatic analysis suggest that FBXO42 may be a favorable prognostic factor for NB patients. However, experimental validation is essential to ascertain the veracity of these findings.

FBXO42 dependent promotion of neuroblastoma cell proliferation through TP53

Upload FBXO42 to the UbiBrowser 2.0 tool to predict potential substrates (Fig. 7A). The 14 predicted potential substrates associated with biological processes such as nucleic acid binding and DNA template transcriptional regulation (Fig. 7B), and are enriched in disease features like the thyroid hormone signaling pathway, Kaposi sarcoma-associated herpesvirus infection, and human papillomavirus infection (Fig. 7C). Subsequently, we overexpressed Flag-FBXO42 in SK-N-SH and SH-SY5Y cell lines to detect potential regulatory molecules. The results showed a downregulation of TP53 protein levels with the overexpression of Flag-FBXO42, while other tumor regulatory factors remained unchanged (Fig. 7D). Colony formation experiments further indicated that Flag-FBXO42 enhanced the proliferative capacity of SK-N-SH cells (Fig. 7E), a result supported by cell viability assays (CCK-8) (Fig. 7F). As an E3 ubiquitin ligase, FBXO42 has been reported to promote the ubiquitination and degradation of TP53³⁸. Combining this information with previous pathway enrichment results (Fig. 5G,6K), we hypothesized that FBXO42 promotes neuroblastoma proliferation through TP53. To test this hypothesis, we used si-RNA to inhibit the expression of FBXO42 and TP53 in the SK-N-SH cell line. Real-time fluorescence quantitative PCR and western blot confirmed the efficiency of inhibition (Fig. 7G–I). Colony formation and cell viability assays revealed that si-FBXO42 effectively suppressed the proliferative capacity of SK-N-SH cells, an effect rescued by the addition of si-TP53 (Fig. 7J,K). These results suggest that the oncogenic role of FBXO42 in neuroblastoma depends on TP53.

Discussion

Ubiquitination modification is a protein modification that plays a regulatory role in complex pathological or physiological processes³⁹, participating in the occurrence and development of various diseases such as tumors, antiviral immunity, and obesity^{40–42}. Previous research on ubiquitination in neuroblastoma has mostly focused on individual ubiquitination-related proteins^{43,44}, with limited studies utilizing systematic exploration of the molecular characteristics and prognostic potential of Ubiquitination-Related Genes (URGs) using proteomic data. In this study, based on proteomic data from 34 neuroblastoma samples, we identified 610 differentially expressed URGs, which were systematically analyzed for potential biological functions. Prognostic features, consisting of six URGs, were constructed through LASSO regression and Cox regression analyses and further integrated with clinical pathological parameters to generate Nomograms. Additionally, we unveiled the immunological and prognostic features of samples assessed as high-risk and low-risk groups based on URG characteristics. Finally, an in-depth exploration of the role of FBXO42 in neuroblastoma was conducted through bioinformatic analysis, cell proliferation assays, and western blotting.

Previous studies on prognostic markers have primarily focused on ferroptosis, autophagy, and immune-related markers^{45–47}, with no research based on ubiquitination-related gene features. In this study, we cataloged 660 E3 ubiquitin ligases and 112 deubiquitinases of the Ubiquitin Proteasome System (UPS). From the proteomic data, we extracted 28 UPS proteins with abnormal expression in N-Myc amplified samples, aiming to explore

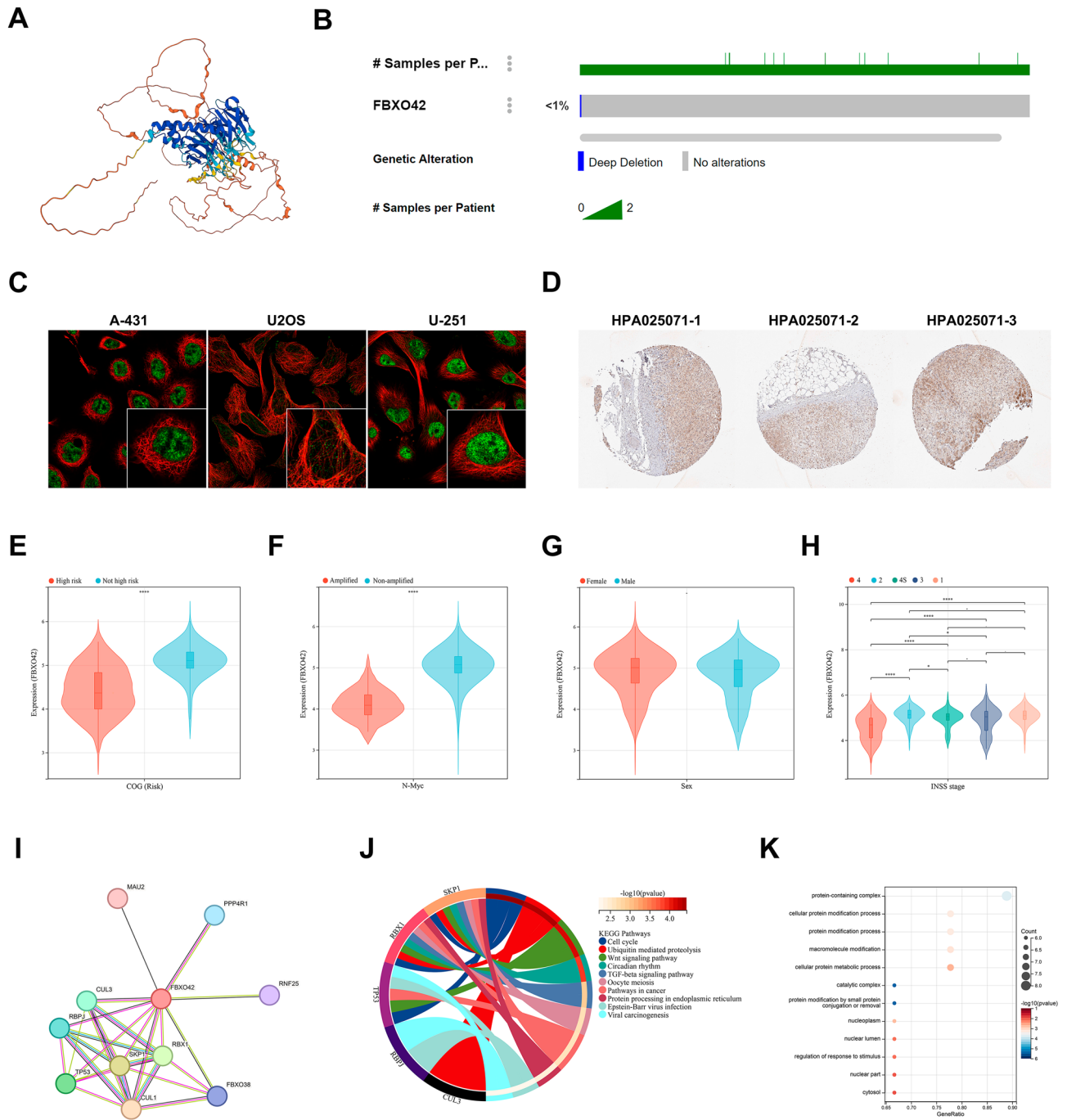


Figure 6. Comprehensive analysis of the role of E3 ubiquitin ligase FBXO42 in neuroblastoma. (A) Predicted protein structure of FBXO42 by alpha fold. (B) Analysis of genetic mutations of FBXO42 in neuroblastoma cohort. (C) Immunofluorescence localization analysis of FBXO42 (green) in A-431, U2OS, and U251 cells. (D) Immunohistochemistry analysis of FBXO42 expression levels in normal human adrenal glands; HPA025071-1 and HPA025071-2 are image IDs in the HPA database. (E–H) Gene expression levels of FBXO42 in different clinical-pathological parameter group samples, including COG risk stratification (E), N-Myc amplification status (F), gender (G), and INSS stage (H). (I) Protein–protein interaction network of FBXO42. (J,K) 11 protein KEGG pathways (J) and GO term enrichment (K) included in the interaction network.

their expression characteristics, prognostic value, and immune therapeutic prognosis in neuroblastoma²⁶. Based on this, a Nomogram incorporating six ubiquitination-related genes (URGs) was constructed, among which UHRF1, FBXO42, UFL1, RNF213, and RBCK1 remain unreported in the context of neuroblastoma. On the other hand, KEAP1 may regulate the cell cycle and apoptosis processes in neuroblastoma through the Nrf2/ARE pathway^{48,49}. The AUC values for 1, 3, and 5 years reached 0.88, 0.93, and 0.95, surpassing previous studies^{23,50}. Moreover, samples assessed as high-risk by the risk model exhibited higher immune scores. Particularly

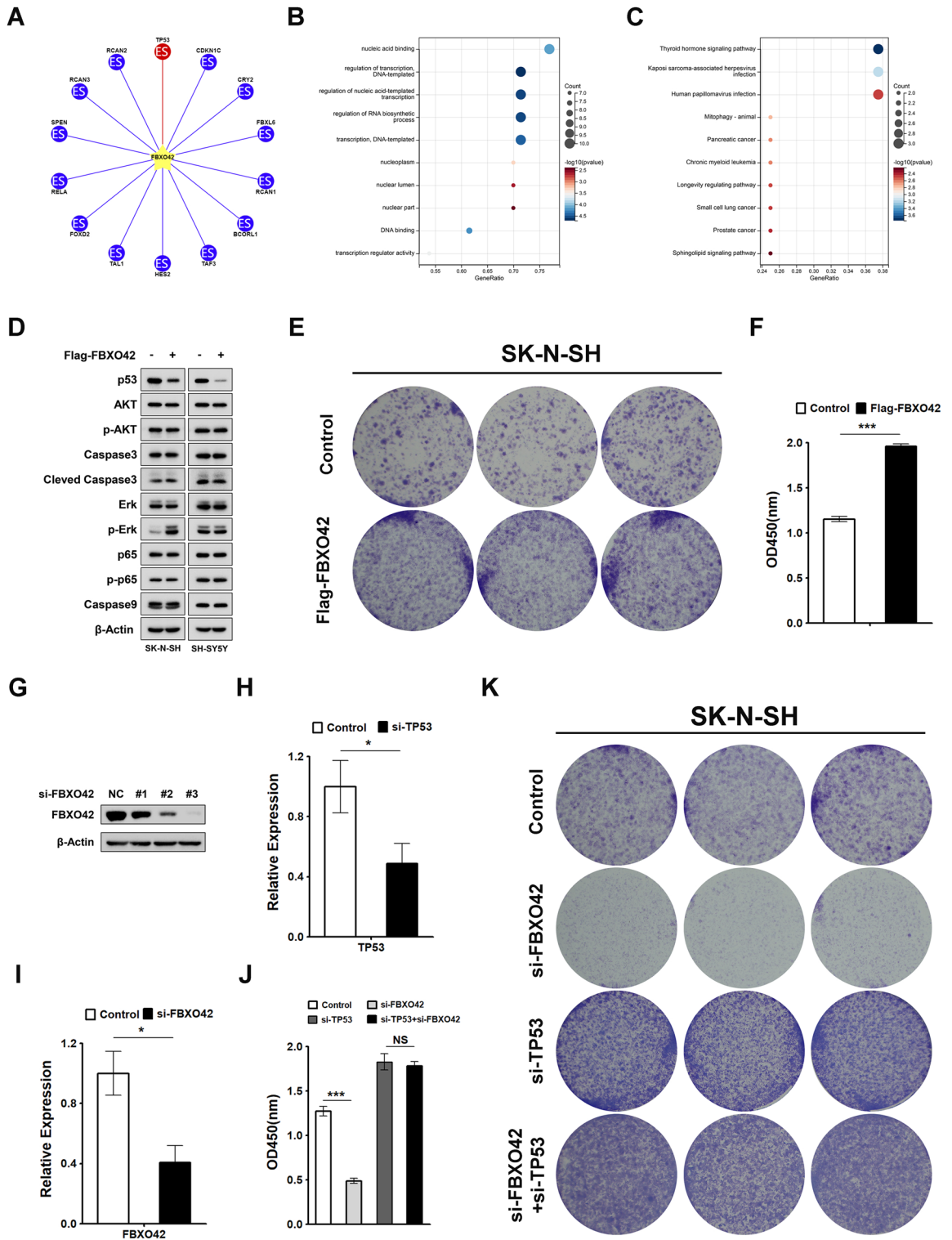


Figure 7. FBXO42 promotes neuroblastoma cell proliferation via TP53 dependence. (A) UbiBrowser 2.0 screening of potential substrate proteins for FBXO42. (B,C) GO (B) and KEGG (C) pathway enrichment analysis of 14 potential substrate proteins. (D) Immunoblotting of SK-N-SH or SH-SY5Y cell lines transfected with Flag-Control or Flag-FBXO42, using the indicated primary antibodies. (E,F) Colony formation assay (E) and CCK-8 (F) detecting the impact of Flag-FBXO42 on SK-N-SH proliferation. (G) SK-N-SH cell lines transfected with si-NC or si-FBXO42 were immunoblotted using the indicated primary antibodies. (H,I) Real-time quantitative PCR validation of si-TP53 (H) and si-FBXO42 (I) knockdown efficiency in SK-N-SH. (J,K) CCK-8 (J) and colony formation assay (K) assessing the effect of si-FBXO42 on SK-N-SH proliferation with or without TP53 inhibition.

noteworthy was the decrease in CD8 T cell infiltration levels and the increase in CD4 T cell infiltration levels, leading to an elevated CD4+/CD8+ ratio. This suggests that the immune function of high-risk samples is in a state of "overactivation," actively engaging in anti-tumor immunity. The CD4+/CD8+ ratio not only reflects the host's immune function status but also serves as an indicator of the response to PD-1 inhibitor therapy^{51,52}. The elevated B cell levels indicate effective recognition of tumor antigens by the body, while the reduced infiltration levels of NK cells suggest a poor prognosis for this population^{53,54}. In conclusion, the risk model established in this study effectively evaluates patients' prognosis and immune therapeutic outcomes, providing valuable insights for clinical treatment strategies.

FBXO42, a member of the F-box protein family, serves as the protein ubiquitin ligase in the SCF complex (comprising SKP1, cullin, and F-box protein)⁵⁵. It recognizes the interaction domain of substrate proteins to interact with targets⁵⁶. Bioinformatics analysis in this study revealed an inverse correlation between FBXO42 and adverse prognosis in patients, suggesting a potential tumor-suppressive role in neuroblastoma. However, subsequent cell experiments indicated that FBXO42 relies on TP53 to promote the proliferation of SK-N-SH cells (MYCN non-amplification). One reason we speculate is that FBXO42 may be negatively regulated by MYCN⁵⁷. Generally, RNA-seq is used for large-scale screening, which can reflect the overall trend of gene expression changes in samples, but it cannot guarantee that the trend of each gene is consistent with RT-PCR^{58–61}. Therefore, the expression level of the target gene in RNA-seq may be inconsistent with the RT-PCR results. Moreover, tumors with elevated proliferation rates may exhibit distinct responses to treatments, such as high-dose chemotherapy and radiation therapy^{62–64}. In certain cancer types, rapidly proliferating tumors are often more vulnerable to cytotoxic therapies due to their heightened metabolic activity and dependency on cell division for growth^{65,66}. Consequently, the heightened proliferation rate induced by elevated FBXO42 expression in neuroblastoma could potentially lead to more favorable responses and anticipated outcomes for neuroblastoma patients undergoing aggressive treatments. Future investigations integrating comprehensive clinical and molecular data from patient cohorts with detailed treatment histories are imperative to elucidate the intricate interplay among these factors and their implications for neuroblastoma treatment strategies and patient prognoses. In conclusion, these findings provide preliminary insights into the prognostic role of FBXO42 in neuroblastoma. Simultaneously, the *in vitro* experiments confirm the pro-proliferative role of FBXO42 and propose its potential dependence on TP53 in playing a crucial role in neuroblastoma.

Certainly, the study has some limitations that should be acknowledged. Firstly, the constructed risk model and identified differences in immune status require further validation with additional clinical samples. Secondly, the phenomenon of FBXO42 relying on TP53 to promote SK-N-SH proliferation necessitates a more in-depth exploration of the molecular mechanisms. This deeper investigation would contribute to explaining the disparities observed in this study between the bioinformatics analysis and experimental results regarding FBXO42.

Conclusion

Our study systematically evaluated the molecular characteristics, prognostic value, and immune functions associated with the ubiquitin–proteasome system in neuroblastoma (NB) through bioinformatics analyses of proteomic and transcriptomic data. We constructed a risk model to predict NB prognosis. Biological evidence supports the role of FBXO42, dependent on TP53, in promoting NB proliferation, providing preliminary evidence for its involvement in the complex biological functions and immune regulation of neuroblastoma. Our findings contribute to unraveling the pathogenic mechanisms of NB, identifying novel biomarkers, and establishing a foundation for developing therapeutic strategies targeting lipid metabolism.

Data availability

Data used in this study can be downloaded from GEO (<https://www.ncbi.nlm.nih.gov/geo/> on December 25, 2023), R2 (<https://hgservers1.amc.nl/cgi-bin/r2/main.cgi>, accessed on December 25, 2023), and UbiBrowser 2.0 (http://ubibrowser.bio-it.cn/ubibrowser_v3/, accessed on December 25, 2023).

Received: 14 January 2024; Accepted: 8 August 2024

Published online: 12 August 2024

References

- Louis, C. U. & Shohet, J. M. Neuroblastoma: Molecular pathogenesis and therapy. *Annu. Rev. Med.* **66**, 49–63 (2015).
- Schleiermacher, G., Janoueix-Lerosey, I. & Delattre, O. Recent insights into the biology of neuroblastoma. *Int. J. Cancer* **135**(10), 2249–2261 (2014).
- Irwin, M. S. *et al.* Revised neuroblastoma risk classification system: A report from the Children's Oncology Group. *J. Clin. Oncol.* **39**(29), 3229–3241 (2021).
- Park, J. R. *et al.* Effect of tandem autologous stem cell transplant vs single transplant on event-free survival in patients with high-risk neuroblastoma: A randomized clinical trial. *JAMA.* **322**(8), 746–755 (2019).
- Matthay, K. K. *et al.* Neuroblastoma. *Nat. Rev. Dis. Primers* **2**, 16078 (2016).
- Halliwell, B. & Wasil, M. Tetracyclines as antioxidants in rheumatoid arthritis: Scavenging of hypochlorous acid. *J. Rheumatol.* **15**(3), 530 (1988).
- Song, L. & Luo, Z. Q. Post-translational regulation of ubiquitin signaling. *J. Cell Biol.* **218**(6), 1776–1786 (2019).
- Weissman, A. M. Themes and variations on ubiquitylation. *Nat. Rev. Mol. Cell Biol.* **2**(3), 169–178 (2001).
- Ikeda, F. & Dikic, I. Atypical ubiquitin chains: new molecular signals. Protein modifications: Beyond the usual suspects' review series. *EMBO Rep.* **9**(6), 536–542 (2008).
- Komander, D., Clague, M. J. & Urbe, S. Breaking the chains: Structure and function of the deubiquitinases. *Nat. Rev. Mol. Cell Biol.* **10**(8), 550–563 (2009).
- Muratani, M. & Tansey, W. P. How the ubiquitin–proteasome system controls transcription. *Nat. Rev. Mol. Cell Biol.* **4**(3), 192–201 (2003).

12. Chen, L., Liu, S. & Tao, Y. Regulating tumor suppressor genes: Post-translational modifications. *Signal Transduct. Target Ther.* **5**(1), 90 (2020).
13. Zhou, Y. *et al.* CCNB1IP1 prevents ubiquitination-mediated destabilization of MYCN and potentiates tumorigenesis of MYCN-amplified neuroblastoma. *Clin. Transl. Med.* **13**(7), e1328 (2023).
14. Dewson, G., Eichhorn, P. J. A. & Komander, D. Deubiquitinases in cancer. *Nat. Rev. Cancer* **23**(12), 842–862 (2023).
15. Tavana, O. *et al.* HAUSP deubiquitinates and stabilizes N-Myc in neuroblastoma. *Nat. Med.* **22**(10), 1180–1186 (2016).
16. Izumi, H. & Kaneko, Y. Trim32 facilitates degradation of MYCN on spindle poles and induces asymmetric cell division in human neuroblastoma cells. *Cancer Res.* **74**(19), 5620–5630 (2014).
17. Becker, K., Marchenko, N. D., Maurice, M. & Moll, U. M. Hyperubiquitylation of wild-type p53 contributes to cytoplasmic sequestration in neuroblastoma. *Cell Death Differ.* **14**(7), 1350–1360 (2007).
18. Yin, T. *et al.* An E3 ubiquitin-proteasome gene signature for predicting prognosis in patients with pancreatic cancer. *Front. Immunol.* **14**, 1332626 (2023).
19. Zhang, J. *et al.* Ubiquitin-proteasome system-based signature to predict the prognosis and drug sensitivity of hepatocellular carcinoma. *Front. Pharmacol.* **14**, 1172908 (2023).
20. Luo, X. *et al.* Identification of a prognostic signature for ovarian cancer based on ubiquitin-related genes suggesting a potential role for FBXO9. *Biomolecules.* **13**(12), 1724 (2023).
21. Tian, X. M. *et al.* A novel cuproptosis-related subtypes and gene signature associates with immunophenotype and predicts prognosis accurately in neuroblastoma. *Front. Immunol.* **13**, 999849 (2022).
22. Shao, F. L., Liu, Q. Q. & Wang, S. Identify potential miRNA-mRNA regulatory networks contributing to high-risk neuroblastoma. *Invest. New Drugs.* **39**(4), 901–913 (2021).
23. Shao, F., Wang, Z. & Wang, S. Identification of MYCN-related gene as a potential biomarker for neuroblastoma prognostic model by integrated analysis and quantitative real-time PCR. *DNA Cell Biol.* **40**(2), 332–347 (2021).
24. Hartlieb, S. A. *et al.* Alternative lengthening of telomeres in childhood neuroblastoma from genome to proteome. *Nat. Commun.* **12**(1), 1269 (2021).
25. Wang, C. *et al.* The concordance between RNA-seq and microarray data depends on chemical treatment and transcript abundance. *Nat. Biotechnol.* **32**(9), 926–932 (2014).
26. Wang, X. *et al.* UbiBrowser 2.0: A comprehensive resource for proteome-wide known and predicted ubiquitin ligase/deubiquitinase-substrate interactions in eukaryotic species. *Nucleic Acids Res.* **50**(D1), D719–D728 (2022).
27. Kanehisa, M. & Goto, S. KEGG: Kyoto encyclopedia of genes and genomes. *Nucleic Acids Res.* **28**(1), 27–30 (2000).
28. Kanehisa, M. Toward understanding the origin and evolution of cellular organisms. *Protein Sci.* **28**(11), 1947–1951 (2019).
29. Kanehisa, M., Furumichi, M., Sato, Y., Kawashima, M. & Ishiguro-Watanabe, M. KEGG for taxonomy-based analysis of pathways and genomes. *Nucleic Acids Res.* **51**(D1), D587–D592 (2023).
30. Subramanian, A. *et al.* Gene set enrichment analysis: A knowledge-based approach for interpreting genome-wide expression profiles. *Proc. Natl. Acad. Sci. USA* **102**(43), 15545–15550 (2005).
31. Liberzon, A. *et al.* Molecular signatures database (MSigDB) 3.0. *Bioinformatics.* **27**(12), 1739–1740 (2011).
32. Yoshihara, K. *et al.* Inferring tumour purity and stromal and immune cell admixture from expression data. *Nat. Commun.* **4**, 2612 (2013).
33. Newman, A. M. *et al.* Robust enumeration of cell subsets from tissue expression profiles. *Nat. Methods* **12**(5), 453–457 (2015).
34. Racle, J., de Jonge, K., Baumgaertner, P., Speiser, D. E. & Gfeller, D. Simultaneous enumeration of cancer and immune cell types from bulk tumor gene expression data. *Elife.* **6**, e26476 (2017).
35. Chen, Y., Li, Z. Y., Zhou, G. Q. & Sun, Y. An Immune-Related Gene Prognostic Index for head and neck squamous cell carcinoma. *Clin. Cancer Res.* **27**(1), 330–341 (2021).
36. Su, Z. *et al.* An investigation of biomarkers derived from legacy microarray data for their utility in the RNA-seq era. *Genome Biol.* **15**(12), 523 (2014).
37. Iasonos, A., Schrag, D., Raj, G. V. & Panageas, K. S. How to build and interpret a nomogram for cancer prognosis. *J. Clin. Oncol.* **26**(8), 1364–1370 (2008).
38. Sun, L. *et al.* Substrate phosphorylation and feedback regulation in JFK-promoted p53 destabilization. *J. Biol. Chem.* **286**(6), 4226–4235 (2011).
39. Pickart, C. M. & Eddins, M. J. Ubiquitin: Structures, functions, mechanisms. *Biochim. Biophys. Acta* **1695**(1–3), 55–72 (2004).
40. Cervia, L. D. *et al.* A ubiquitination cascade regulating the integrated stress response and survival in carcinomas. *Cancer Discov.* **13**(3), 766–795 (2023).
41. Li, H. *et al.* Secreted LRPAP1 binds and triggers IFNAR1 degradation to facilitate virus evasion from cellular innate immunity. *Signal Transduct. Target Ther.* **8**(1), 374 (2023).
42. Lu, X. *et al.* UBE2M-mediated neddylation of TRIM21 regulates obesity-induced inflammation and metabolic disorders. *Cell Metab.* **35**(8), 1390–405 e8 (2023).
43. Bedekovics, T. *et al.* USP24 is a cancer-associated ubiquitin hydrolase, novel tumor suppressor, and chromosome instability gene deleted in neuroblastoma. *Cancer Res.* **81**(5), 1321–1331 (2021).
44. Gu, Y. *et al.* The deubiquitinating enzyme UCHL1 is a favorable prognostic marker in neuroblastoma as it promotes neuronal differentiation. *J. Exp. Clin. Cancer Res.* **37**(1), 258 (2018).
45. Meng, X., Li, H., Fang, E., Feng, J. & Zhao, X. Comparison of Stage 4 and Stage 4s neuroblastoma identifies autophagy-related gene and lncRNA signatures associated with prognosis. *Front. Oncol.* **10**, 1411 (2020).
46. Hu, J. *et al.* Integrative analysis of multi-omics data for discovery of ferroptosis-related gene signature predicting immune activity in neuroblastoma. *Front. Pharmacol.* **14**, 1162563 (2023).
47. Ma, K. *et al.* A signature based on five immune-related genes to predict the survival and immune characteristics of neuroblastoma. *BMC Med. Genom.* **15**(1), 242 (2022).
48. Ren, J. *et al.* Lupiwighteone induces cell cycle arrest and apoptosis and activates the Nrf2/ARE pathway in human neuroblastoma cells. *Biomed. Pharmacother.* **69**, 153–161 (2015).
49. Filomeni, G., Piccirillo, S., Rotilio, G. & Ciriolo, M. R. p38(MAPK) and ERK1/2 dictate cell death/survival response to different pro-oxidant stimuli via p53 and Nrf2 in neuroblastoma cells SH-SY5Y. *Biochem. Pharmacol.* **83**(10), 1349–1357 (2012).
50. Chen, W., Lin, P., Bai, J., Fang, Y. & Zhang, B. Establishment and validation of a nomogram to predict cancer-specific survival in pediatric neuroblastoma patients. *Front. Pediatr.* **11**, 1105922 (2023).
51. Xu, S. *et al.* Association of the CD4(+)/CD8(+) ratio with response to PD-1 inhibitor-based combination therapy and dermatological toxicities in patients with advanced gastric and esophageal cancer. *Int. Immunopharmacol.* **123**, 110642 (2023).
52. Duchemann, B. *et al.* CD8(+)/PD-1(+) to CD4(+)/PD-1(+) ratio (PERLS) is associated with prognosis of patients with advanced NSCLC treated with PD-(L)1 blockers. *J. Immunother. Cancer* **10**(2), e004012 (2022).
53. Wu, S. Y., Fu, T., Jiang, Y. Z. & Shao, Z. M. Natural killer cells in cancer biology and therapy. *Mol. Cancer* **19**(1), 120 (2020).
54. Cozar, B. *et al.* Tumor-infiltrating natural killer cells. *Cancer Discov.* **11**(1), 34–44 (2021).
55. Skaar, J. R., Pagan, J. K. & Pagano, M. Mechanisms and function of substrate recruitment by F-box proteins. *Nat. Rev. Mol. Cell Biol.* **14**(6), 369–381 (2013).
56. Jin, J. *et al.* Systematic analysis and nomenclature of mammalian F-box proteins. *Genes Dev.* **18**(21), 2573–2580 (2004).

57. Veas-Perez de Tudela, M., Delgado-Esteban, M., Cuende, J., Bolanos, J. P. & Almeida, A. Human neuroblastoma cells with MYCN amplification are selectively resistant to oxidative stress by transcriptionally up-regulating glutamate cysteine ligase. *J. Neurochem.* **113**(4), 819–825 (2010).
58. Zhang, W. *et al.* Comparative transcriptomic analysis of immune responses of the migratory locust, *Locusta migratoria*, to challenge by the fungal insect pathogen, *Metarhizium acridum*. *BMC Genom.* **16**, 867 (2015).
59. Teng, M. *et al.* A benchmark for RNA-seq quantification pipelines. *Genome Biol.* **17**, 74 (2016).
60. Robert, C. & Watson, M. Errors in RNA-Seq quantification affect genes of relevance to human disease. *Genome Biol.* **16**(1), 177 (2015).
61. Everaert, C. *et al.* Benchmarking of RNA-sequencing analysis workflows using whole-transcriptome RT-qPCR expression data. *Sci. Rep.* **7**(1), 1559 (2017).
62. Pawlik, T. M. & Keyomarsi, K. Role of cell cycle in mediating sensitivity to radiotherapy. *Int. J. Radiat. Oncol. Biol. Phys.* **59**(4), 928–942 (2004).
63. Baskar, R., Dai, J., Wenlong, N., Yeo, R. & Yeoh, K. W. Biological response of cancer cells to radiation treatment. *Front. Mol. Biosci.* **1**, 24 (2014).
64. Perez-Gonzalez, A., Bevant, K. & Blanpain, C. Cancer cell plasticity during tumor progression, metastasis and response to therapy. *Nat. Cancer.* **4**(8), 1063–1082 (2023).
65. Liang, R. *et al.* Seleno-amino Acid metabolism reshapes the tumor microenvironment: From cytotoxicity to immunotherapy. *Int. J. Biol. Sci.* **20**(7), 2779–2789 (2024).
66. Das, C. *et al.* A prismatic view of the epigenetic-metabolic regulatory axis in breast cancer therapy resistance. *Oncogene* **43**, 1727 (2024).

Acknowledgements

Thanks to all the staff who contributed to the GEO, R2 and UbiBrowser databases. Thanks to the reviewers and editors for their sincere comments.

Author contributions

J. Z. and Y.D. wrote the main manuscript text; J. Z., Q.L., and X.D. performed the cell experiments; J. Z. and L.P. performed the data analysis and visualization. Y.Z. and J.S. performed the data collection. All authors reviewed the manuscript.

Competing interests

The authors declare no competing interests.

Additional information

Supplementary Information The online version contains supplementary material available at <https://doi.org/10.1038/s41598-024-69760-2>.

Correspondence and requests for materials should be addressed to Y.D.

Reprints and permissions information is available at www.nature.com/reprints.

Publisher's note Springer Nature remains neutral with regard to jurisdictional claims in published maps and institutional affiliations.

Open Access This article is licensed under a Creative Commons Attribution-NonCommercial-NoDerivatives 4.0 International License, which permits any non-commercial use, sharing, distribution and reproduction in any medium or format, as long as you give appropriate credit to the original author(s) and the source, provide a link to the Creative Commons licence, and indicate if you modified the licensed material. You do not have permission under this licence to share adapted material derived from this article or parts of it. The images or other third party material in this article are included in the article's Creative Commons licence, unless indicated otherwise in a credit line to the material. If material is not included in the article's Creative Commons licence and your intended use is not permitted by statutory regulation or exceeds the permitted use, you will need to obtain permission directly from the copyright holder. To view a copy of this licence, visit <http://creativecommons.org/licenses/by-nc-nd/4.0/>.

© The Author(s) 2024